CFD Modeling and Analysis of a Planar Anode Supported Intermediate Temperature Solid Oxide Fuel Cell

N. O. Lemcoff*[1], M. Tweedie[2]
1. Rensselaer Polytechnic Institute Hartford, Hartford, CT, USA
2. Enthone, West Haven, CT, USA
*Corresponding author: lemcon@rpi.edu

Abstract: The objective of this study is to analyze a planar anode-supported intermediate temperature solid oxide fuel cell operating on syngas fuel at 750°C. The effects of varying simulated syngas fuel inlet compositions on species and temperature distributions, water gas shift reaction rate, potential for carbon formation and electrochemistry were considered. A 2-D COMSOL model was developed which included separate defined electrochemical reaction layers on either side of the electrolyte, where both chemical reforming and electrochemical reactions simultaneously occurred. The CFD model consisted of 5 submodels utilizing the Navier Stokes and continuity equations for momentum transport, Maxwell-Stefan model and Knudsen diffusion for mass transport, energy equation for heat transfer, a chemical reforming model, and an electrochemical model considering distributed charge transfer over the cell, including Butler-Volmer type kinetics. Resulting model polarization curves showed good agreement with experimental data, and the best simulated performance was found for high fuel inlet concentrations of hydrogen and carbon monoxide resulting in a maximum power density of 720W/m^2.

Keywords: Solid Oxide Fuel Cell, Syngas

1. Introduction

Fuel cells are promising alternative energy technologies which convert fuel and oxygen to electricity, water and carbon dioxide. Solid oxide fuel cells (SOFCs) are a class of high temperature fuel cells operating between 600°C to 1000°C that use hydrogen or hydrocarbons as the fuel and air as the oxidant. This type of fuel cell utilizes porous ceramic electrodes for the anode and cathode, separated by a solid ceramic electrolyte. The structure of the SOFC is commonly referred to as the PEN or positive-electrode/ electrolyte/ negative-electrode structure. The two primary configurations of SOFCs are tubular and planar. Due to limitations in the performance of tubular SOFCs, namely that tubular stack designs have demonstrated low specific power densities, the focus in recent years has been optimizing the planar design configurations [1].

In the planar type of solid oxide fuel cells, the general configuration consists of an interconnect plate, an air/fuel flow field, the PEN structure, the alternate air/fuel flow field and an alternate interconnect plate. The interconnect plates within a fuel cell stack are typically fabricated with flow fields on either side, such that only one interconnect plate is present in repeating cell units. In anode supported planar SOFCs, the most common materials utilized today consist of a yttria-stabilized zirconia (YSZ) electrolyte, and porous ceramic metallic composites (cermets), including nickel/zirconia (Ni-YSZ) anode and strontium doped $LaMnO_3$ (LSM) mixed with YSZ composite cathode [2].

Due to the high operating temperatures and potential for large thermal gradients in SOFCs, challenges such as material degradation and cracking, high cost of operation, coking and reduced efficiencies have resulted in continual room for design and process optimizations.

Operating at reduced temperatures to alleviate some of these issues, intermediate temperature direct internal reforming (IT-DIR) solid oxide fuel cells have been studied by several groups [3-5]. These lower temperature fuel cells typically operate between 550°C and 800°C. To reduce the thermal stress and coke formation from large temperature gradients in the cell, driven by the highly endothermic methane steam reforming reaction at the inlet, several approaches have been investigated including increasing the inlet steam to carbon ratio [6], impregnating the anode with copper [7] and utilizing alternative methane-free fuels such as biogas or syngas [8].

Previous multiphysics modeling of SOFCs has included both two and three dimensional numerical and CFD simulations. Generally, the more predominant models define the electrochemical reactions as occurring at the electrode-electrolyte interface. However, the electrochemical reactions actually occur both at the interface and in the electrode [9]. Therefore, to enhance the predictive capability of a single cell level study, reactions in the electrode should also be considered.

Additionally, it has been found that the overall electrochemical reaction rate can vary up to 50% with the oxidation of CO when compared with only the oxidation of hydrogen [10]. Therefore, for model accuracy, both hydrogen oxidation and CO oxidation should be included in a cell level study where anode species composition could contain notable amounts of CO, such as in pre-reformed hydrocarbon feeds, syngas feeds, or fuel cells with internal reforming. Increasingly CO oxidation is being considered in cell level modeling [3-4, 8, 10-13].

2. Methodology

2.1 Model Development

This study considered a two dimensional CFD model of a planar anode-supported IT-DIR SOFC with composite Ni-YSZ anode and composite LSM-YSZ cathode. In the model domain shown in Figure 1, there are a total of nine distinct layers with dimensions defined in Table 1. The model includes distinct active catalyst electrochemical reaction layers (ERLs) to replicate the location of the electrochemically active zone within the electrodes near the electrode-electrolyte boundary.

Table 1. Cell Dimensions (mm)

Cell length	100	Anode ERL Height	0.03
Cell height	3.31	Air channel height	1.0
Interconnect Height	0.5	Cathode BL Height	0.05
Fuel channel Height	0.6	Cathode ERL Height	0.01
Anode BL Height	0.6	Electrolyte Height	0.02

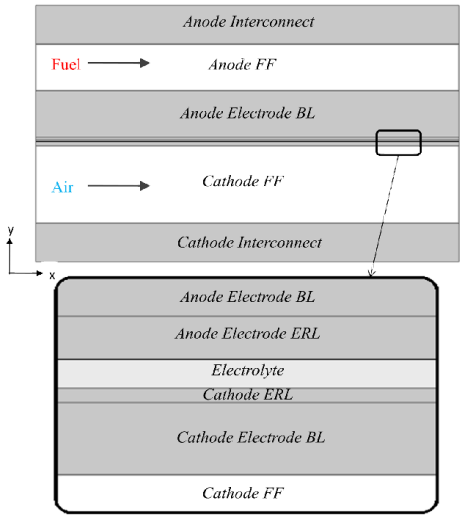

Figure 1. Single Cell Model Domain

The commercially available software COMSOL was used to model the domain. The model consists of conservation equations for mass, momentum, species, charge and energy. Using the Free and Porous Media Flow Module, Navier-Stokes equations were utilized to model the flow in the anode and cathode flow fields, and the Brinkman equations were utilized to model the flow in the porous electrodes. For the mass balances, the Transport of Concentrated Species Module was used. It includes Maxwell-Stefan diffusion, where species transfer and kinetic rate equations were considered for both the chemical and electrochemical reactions. The energy balance was incorporated through the use of the Heat Transfer in Fluids Module. For the electronic and ionic charge balance, the appropriate distributed charge transfer equations were entered manually into the Mathematics Module using Poisson's equations. All other definitions and equations utilized were manually entered as defined variables applied into the model.

The model mesh consisted of 34,400 elements in total, with a higher density of elements at the inlet and outlet of the cell, in the ERLs and in the electrolyte layer. To achieve the varying distribution along the cell, the length was divided into 400 elements with an arithmetic sequence, symmetric distribution (in reverse direction) using an element ratio of 0.01. The remaining distributions for each subdomain in

the vertical direction utilized a fixed number of evenly distributed elements.

To solve the system, a segregated step PARDISO solver was used, with an overall relative tolerance of 0.001. A consistent stabilization tuning parameter C_k=0.4 was implemented in the model along with an automatic highly nonlinear damping method, terminating based on tolerance for each set of variables solved for. The order of the segregated steps included; 1) velocity and pressure 2) electronic/ionic potentials 3) cathode species distribution 4) anode species distribution and 5) temperature. To generate the polarization curves, parametric voltage steps were applied in increments of 0.05 from -0.95V to -0.4V.

2.2 Physical Parameters

The physical properties, electrochemical parameters and thermal parameters utilized in the model are shown in Table 2.

Table 2. Physical Properties [14]

	Anode	Cathode
Permeability (m^2)	2.42 x 10^{-14}	2.54 x 10^{-14}
Porosity	0.489	0.515
Pore Diameter (μm)	0.971	1
Electronic/Ionic/Pore Tortuosity	7.53, 8.48, 1.80	7.53, 3.40, 1.80
Electronic/Ionic Volume Fraction	0.257, 0.254	0.232, 0.253
Electronic/Ionic Reactive Surface Area per Unit Volume (m^2/m^3)	3.97x10^6, 7.93x10^6	3.97x10^6, 7.93x10^6
Solid Thermal Conductivity (W/m-K)	11	6
Solid Specific Heat Capacity (J/kg-K)	450	430
Solid Density (kg/m^3)	3310	3030
	Electrolyte	Interconnect
Thermal Conductivity (W/m-K)	2.7	20
Specific Heat Capacity (J/kg-K)	470	550
Solid Density (kg/m^3)	5160	3030

2.3 Simulation Conditions

The cell was simulated using an inlet temperature of 1023K, cathode inlet velocity of 6.5 m/s, anode inlet velocity of 0.5 m/s, outlet pressure of 1.0 atm and operating voltage between 0.4 and 0.95V. This study considered various fuel inlet compositions representing typical ranges for syngas fuels, as shown in Table 3.

Table 3. Simulated Fuel Feed Mole Fractions

Case	1	2	3	4	5
H_2	0.30	0.30	0.20	0.30	0.30
H_2O	0.07	0.17	0.27	0.07	0.07
CO	0.50	0.40	0.40	0.40	0.40
CO_2	0.10	0.10	0.10	0.10	0.20
CH_4	0.01	0.01	0.01	0.01	0.01
N_2	0.02	0.02	0.02	0.12	0.02

3. Theory

3.1 Momentum Transfer

For the open flow fields in the cell, including the fuel and air flow channels, the Continuity and Navier-Stokes equations were utilized, considering compressible flow and steady state conditions. For the flow in the porous electrodes (and corresponding electrode reaction layers) the Stokes-Brinkman equations were utilized, which neglects the initial term in the Brinkman equations due to very low Reynolds number.

The boundary conditions include no slip conditions at the walls, and specified inlet velocities at the anode and cathode. The dynamic viscosity of the gas mixtures was calculated using the Wilke and Heming and Zipperer methods [15]. Mixture density was calculated based on ideal gas behavior.

3.2 Mass Transfer

The molecular mass transport equations included calculated Maxwell-Stefan diffusivity matrix values to model the steady state species transport in the fuel cell flow fields and electrodes. The Fuller expression was used to calculate the Maxwell-Stefan diffusivity values for the flow fields [16].

$$D_{ij}^{MS} = \frac{1.43x10^{-2}T^{1.75}}{pM_{ij}^{1/2}\left[V_i^{1/3} + V_j^{1/3}\right]^2} \quad (1)$$

$$M_{ij} = \frac{2}{\frac{1}{M_i} + \frac{1}{M_j}} \quad (2)$$

The Dusty Gas Model utilizing an effective diffusivity value was applied in the porous media.

$$D_{ij}^{eff} = \frac{\varepsilon}{\tau_{pore}}\left(\frac{1}{D_{ij}^{MS}} + \frac{1}{D_i^{Kn}}\right)^{-1} = \frac{\varepsilon}{\tau_{pore}}\frac{D_{ij}^{MS}D_{ij}^{Kn}}{D_{ij}^{Kn} + D_{ij}^{MS}} \quad (3)$$

$$D_{ij}^{Kn} = r_{pore}\frac{2}{3}x10^{-4}\sqrt{\frac{8RT}{\pi\bar{M}_{ij}}} = 48.5x10^{-4}d_{\ pore}\sqrt{\frac{T}{\bar{M}_{ij}}} \quad (4)$$

$$\bar{M}_{ij} = (M_i + M_j)/2 \quad (5)$$

Thermal diffusion coefficient data for multicomponent mixtures for the gaseous mixture in the anode is currently unavailable. Therefore, the thermal diffusion coefficient was neglected in this study. Boundary conditions include mass flux in/out of the cell via the flow fields and the inflow species concentrations were predefined mass fractions.

3.3 Heat Transfer

For the heat transfer in the gas flow fields, the following form of the energy equation was used. The fluid mixture specific heat capacities were determined based on ideal gas mixtures such that they were a function of temperature.

$$\rho C_p \boldsymbol{u}\nabla T - \nabla(\lambda\nabla T) = Q \quad (6)$$

To determine the thermal conductivity of the fluid mixtures, the method of Wassiljewa was utilized with the Mason and Saxena modification as suggested by Todd and Young [15-16]. In the electrodes, a modified version of the energy equation was utilized.

$$\rho C_p^{eff}\boldsymbol{u}\nabla T - \nabla(\lambda^{eff}\nabla T) = Q \quad (7)$$

$$\lambda^{eff} = \varepsilon\lambda_{fluid} + (1-\varepsilon)\lambda_{solid} \quad (8)$$

$$C_p^{eff} = \varepsilon C_{p,fluid} + (1-\varepsilon)C_{p,solid} \quad (9)$$

For the electrolyte and interconnects only conduction heat transfer was considered.

$$-\nabla(\lambda\nabla T) = Q \quad (10)$$

The heat generated due to the chemical reactions, electrochemical reactions and activation polarizations is shown for each subdomain in Table 4.

Table 4. Heat Source Terms

Anode FF	$Q = (-\Delta H_{298}^{WGS} * \dot{r}_{\ WGS})$	(11)
Anode BL	$Q = (-\Delta H_{298}^{WGS} * \dot{r}_{\ WGS})$	(12)
Anode ERL	$Q = (-\Delta H_{298}^{WGS} * \dot{r}_{\ WGS}) + j_{H2}A_v\left(\frac{-\Delta H_{H2}}{2F} - E_{cell}\right) + j_{CO}A_v\left(\frac{-\Delta H_{CO}}{2F} - E_{cell}\right) + \eta_{act,a,H2}j_aA_v + \eta_{act,a,CO}j_aA_v$	(13)
Electrolyte	Q = 0	(14)
Cathode ERL	$Q = \eta_{act,c,O2}j_cA_v$	(15)
Cathode BL	Q = 0	(16)
Cathode FF	Q = 0	(17)
Interconnects	Q = 0	(18)

3.4 Chemical Reactions

In this study the fuel composition consisted primarily of carbon monoxide and hydrogen. Thus, the primary reaction considered included the water gas shift reaction (WGS). Haberman and Young kinetics were implemented in this model [17]. The catalyzed methane steam reforming reaction was considered for inclusion in this model however the extremely fast reaction rates prevented model convergence [14].

$$CO + H_2O \leftrightarrow H_{\ 2} + CO\Delta H_{\ 298} = -41.2kJ/mol \quad (19)$$

The probability for carbon formation via the Boudouard reaction (20) and reaction (21) was additionally assessed based on the probability of carbon activity at a value greater than one [18].

$$2CO \leftrightarrow CO_2 + C \quad (20)$$

$$CO + H_2 \leftrightarrow H_2O + C \quad (21)$$

$$\alpha_{carbon,CO} = 5.744x10^{-15}exp\left(\frac{20634}{T}\right)\frac{p_{CO}^2}{p_{CO_2}} \quad (22)$$

$$\alpha_{carbon,CO-H_2} = 3.173x10^{-13}exp\left(\frac{16318}{T}\right)\frac{p_{CO}p_{H_2}}{p_{H_2O}} \quad (23)$$

3.5 Electrochemical Reactions

The electrochemical reactions included hydrogen and carbon monoxide oxidation and oxygen reduction.

$$H_2 + O^{2-} \rightarrow H_2O + 2e^- \quad (24)$$

$$CO + O^{2-} \rightarrow CO_2 + 2e^- \quad (25)$$

$$1/2\,O_2 + 2e^- \rightarrow O^{2-} \quad (26)$$

A distributed charge transfer approach was taken to simulate the ion and charge transport across the cell. The summary of charge transfer equations were shown in Table 5.

Table 5. Charge Transfer Equations

Electrode BLs	$\nabla \cdot \left(-\sigma_{el,ba}^{eff} \nabla \phi_{el}\right) = 0$	(27)
	$\nabla \cdot \left(-\sigma_{el,bc}^{eff} \nabla \phi_{el}\right) = 0$	(28)
Anode ERL	$\nabla \cdot \left(-\sigma_{el,a}^{eff} \nabla \phi_{el}\right) = -j_a A_v$	(29)
	$\nabla \cdot \left(-\sigma_{io}^{eff} \nabla \phi_{io}\right) = j_a A_v$	(30)
Cathode ERL	$\nabla \cdot \left(-\sigma_{el,c}^{eff} \nabla \phi_{el}\right) = j_c A_v$	(31)
	$\nabla \cdot \left(-\sigma_{io}^{eff} \nabla \phi_{io}\right) = -j_c A_v$	(32)
Electrolyte	$\nabla \cdot \left(-\sigma_{io} \nabla \phi_{io}\right) = 0$	(33)

The cell voltage was satisfied by setting boundary conditions such that the electrical potential $\phi_{el} = 0$ in the cathode backing layer, and $\phi_{el} = E_{cell}$ in the anode backing layer. For the study, the cell voltage was then varied from -0.95 to -0.4.

Butler-Volmer type kinetics was used for the electrochemical reactions.

$$j_{H2} = j_{o,a,H2}\left[\exp\left(\frac{2F\eta_{\ act,a,H2}}{RT}\right) - exp\left(\frac{-F\eta_{\ act,a,H2}}{RT}\right)\right] \quad (34)$$

$$j_{o,a,H2} = 2.1 \cdot 10^{11} \frac{RT}{F}\left(\frac{p_{H2O}}{1.78 \cdot 10^9 p_{H2}}\right)^{0.266} exp\left(-\frac{1.2 \cdot 10^5}{RT}\right) \quad (35)$$

$$j_{CO} = j_{o,a,CO}\left[\exp\left(\frac{2F\eta_{\ act,a,CO}}{RT}\right) - exp\left(\frac{-F\eta_{\ act,a,CO}}{RT}\right)\right] \quad (36)$$

$$j_{o,a,CO} = 0.84 \cdot 10^{11} \frac{RT}{F}\left(\frac{p_{CO_2}}{1.63 \cdot 10^9 p_{CO}}\right)^{0.266} exp\left(-\frac{1.2 \cdot 10^5}{RT}\right) \quad (37)$$

$$j_{O2} = j_{o,c,O2}\left[\exp\left(\frac{-2F\eta_{\ act,c,O2}}{RT}\right) - exp\left(\frac{2F\eta_{\ act,c,O2}}{RT}\right)\right] \quad (38)$$

$$j_{o,c,O2} = 0.25 \cdot 10^{11} \frac{RT}{F}\left(p_{O_2}\right)^{0.5} exp\left(-\frac{1.3 \cdot 10^5}{RT}\right) \quad (39)$$

Similar SOFC modeling utilizing distributed charge transfer sets the equilibrium potentials based on an anode reference state set to zero. However, in this study, the reversible Nernst potentials combined with electrode reference potentials used by Suwanwarangkul et al. were implemented [8].

$$\eta_{act,a,H2} = \phi_{el,a} - \phi_{io,a} - E_{a,H2}^{rev} \quad (40)$$

$$E_{a,H2}^{rev} = \frac{RT}{2F}\ln\left(\frac{p_{H_2O}}{1.78 \cdot 10^9 p_{H2}}\right) \quad (41)$$

$$\eta_{act,a,CO} = \phi_{el,a} - \phi_{io,a} - E_{a,CO}^{rev} \quad (42)$$

$$E_{a,CO}^{rev} = \frac{RT}{2F}\ln\left(\frac{p_{CO_2}}{1.63 \cdot 10^9 p_{CO}}\right) \quad (43)$$

$$\eta_{act,c,O2} = \phi_{el,c} - \phi_{io,c} - E_{c,O2}^{rev} \quad (44)$$

$$E_{c,O2}^{rev} = \frac{RT}{4F}\ln(p_{O2}) \quad (45)$$

The ohmic losses in the cell were represented by effective conductivity equations [4, 9, 14].

Table 6. Subdomain Effective Conductivities

Electrode BLs	$\sigma_{el,ba}^{eff} = \sigma_{el,a}\left(\frac{1-\varepsilon_a}{\tau_{el,a}}\right)$	(46)
	$\sigma_{el,bc}^{eff} = \sigma_{el,c}\left(\frac{1-\varepsilon_c}{\tau_{el,c}}\right)$	(47)
Anode ERL	$\sigma_{el,a}^{eff} = \sigma_{el,a}\left(\frac{1-\varepsilon_a}{\tau_{el,a}}\right)V_{el,a}$	(48)
	$\sigma_{io,a}^{eff} = \sigma_{io}\left(\frac{1-\varepsilon_a}{\tau_{io,a}}\right)V_{io,a}$	(49)
Cathode ERL	$\sigma_{el,c}^{eff} = \sigma_{el,c}\left(\frac{1-\varepsilon_c}{\tau_{el,c}}\right)V_{el,c}$	(50)
	$\sigma_{io,c}^{eff} = \sigma_{io}\left(\frac{1-\varepsilon_c}{\tau_{io,c}}\right)V_{io,c}$	(51)
Electrolyte	σ_{io}	(52)

4. Results

Initial studies indicated that high reaction rates introduced instability into the model, resulting in non-convergence. Thus, in order to attain convergence for all cases, a dampening constant of 0.05% was applied to the electrochemical species and electrochemical heat generation source term equations (Figure 2).

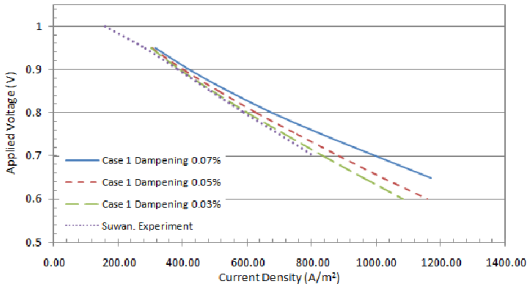

Figure 2. Effect of varying dampening factor

The variation in species composition along the length of the cell is due to the water gas shift chemical reaction, as well as the electrochemical oxidation and reduction reactions (Figure 3).

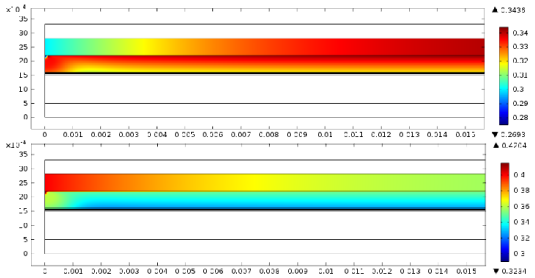

Figure 3. Case 2 inlet (a) H_2 mole fraction (b) CO mole fraction at 0.7V

At the very inlet to the electrodes, slight pressure increases and mass diffusion limitations at the modeled permeability also drive a slight change in the species mole fractions (Figure 4).

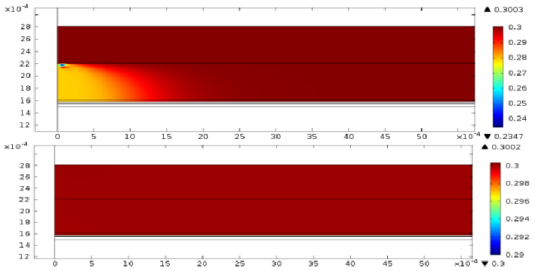

Figure 4. H2 Mole fraction distribution for permeability (a) $2.42x10^{-14}$ and (b) $2.42x10^{-5}$

There was a very small change in the WGS reaction rate at different applied voltages for the same case. However, as expected, there was a significant increase in the reaction rate as the water content was increased in case 3 (Figure 5).

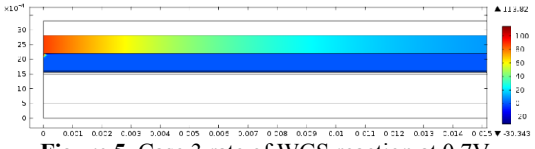

Figure 5. Case 3 rate of WGS reaction at 0.7V

At each applied voltage, the probability of carbon formation was assessed. It was observed that in all cases, the carbon activity did not exceed a value of one. The highest carbon activities occurred in case 1, at the highest applied cell voltage of 0.95V (Figure 6).

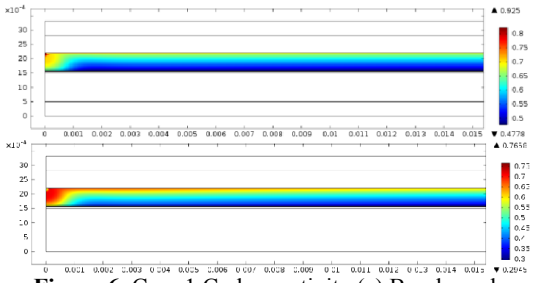

Figure 6. Case 1 Carbon activity (a) Boudouard reaction (b) reaction (21)

The highest temperature increases over the length of the cell were observed in case 1 when the lowest voltage was applied. This is likely due to the high concentrations of H_2 and CO at the inlet, which results in an increase in the electrochemical heat generation (Figure 7).

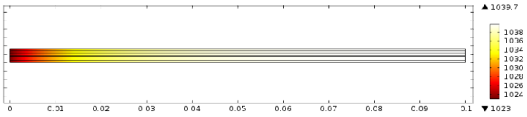

Figure 7. Case 1 temperature at 0.4V

The polarization curves for each case run are shown in Figure 8. The majority of the electrochemical reaction was found to occur at the ERL-electrolyte interface (Figure 9).

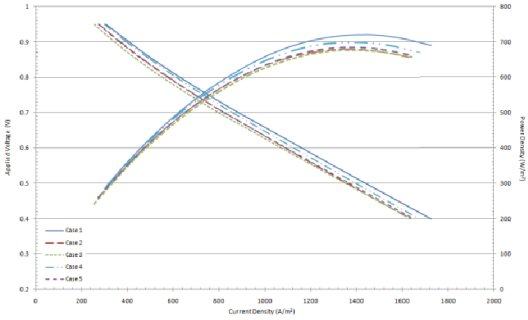

Figure 8. Case 1 to 5 Polarization Curves

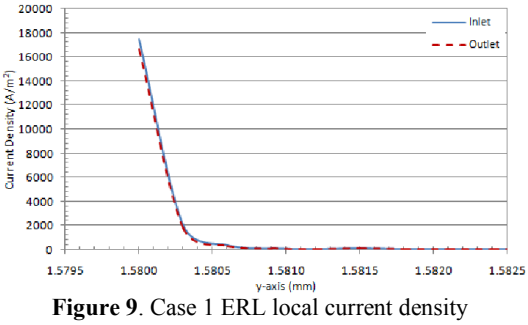

Figure 9. Case 1 ERL local current density

When comparing the resulting polarization curves to experimental data it was found that the current model aligns well with the experimental data taken from Suwanwarungkul et al. [8], as shown in Figure 10.

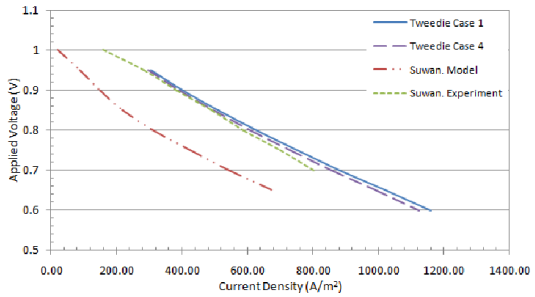

Figure 10. Comparison with experimental data

5. Conclusions

This study examined the effects of the composition of simulated syngas fuel on the performance of an IT-SOFC operating with an inlet temperature of 750°C. It was shown that as the applied cell voltage is decreased, and the cell current density increases, the heat generation within the cell increases, and the probability for carbon formation decreases. Observable inlet mass diffusion limitations were present when a permeability value of ~$2.5 \times 10^{-14} m^2$ was utilized for the porous electrodes. However, these effects only occurred in the initial 0.2% of total cell length.

Increasing the water content in the fuel decreased the probability for carbon formation, although in this study carbon formation would not be expected to occur due to lack of large temperature gradients, and the cell not being operated below 250 A/m^2. The water gas shift reaction showed the most activity at the inlet of the cell, and was found to operate reversibly with higher amounts of CO_2 in the fuel.

When analyzing the effect of the different feed compositions, it was found that the inlet concentrations of CO and H_2 had the most significant effect on cell performance. This resulted in case 1 having the best performance, with a maximum power density of $720 W/m^2$, and case 3 the lowest performance, with a maximum power density of 676 W/m^2. Interestingly, case 4 which contained a larger balance of nitrogen performed better than cases 2, 3 and 5. Cases 2 and 5 in which 10% of the feed was changed from water to carbon dioxide showed similar performance.

6. References

1. T. L. Cable and S. W. Sofie, *Journal of Power Sources*, **174**, 221-227 (2007)
2. P. Aguiar, C. S. Adjiman, and N. P. Brandon, *Journal of Power Sources*, **138**, 120-136 (2004)
3. T. X. Ho, P. Kosinski, A. C. Hoffman, and A. Vik, *International Journal of Hydrogen Energy*, **34**, 3488-3499 (2009)
4. M. Andersson, J. Yuan, and B. Sunden, *Journal of Power Sources*, **232**, pp. 42-54 (2013)
5. D. H. Jeon, *Electrochimica Acta* , **54**, 2727-2736 (2009)
6. J. Meusinger, E. Riensche, and U. Stimming, *Journal of Power Sources*, **71**, 315-320 (1998)
7. M. Boder and R. Dittmeyer, *Journal of Power Sources*, **155**, 13-22, (2006)
8. R. Suwanwarangkul et al., *Journal of Power Sources*, **161**, 308-322 (2006)
9. M. M. Hussain and X. Li. Dincer, *Journal of Power Sources* , **189**, 916-928 (2009)
10. J. Park, P. Li, and J. Bae, *International Journal of Hydrogen Energy*, **37**, 8512-8531 (2012)
11. L. Andreassi, C. Toro, and S. Ubertini, *Journal of Fuel Cell Science and Technology*, **6**, 021307-1 (2009)
12. O. Razbani, M. Assadi, and M. Andersson, *International Journal of Hydrogen Energy*, **38**, 10068-10080 (2013)
13. H. Iwai, Y. Yamamoto, M. Saito, and H. Yoshida, *Energy*, **36**, 2225-2234 (2011)
14. M. Tweedie, *CFD Modeling and Analysis of a Planar Anode Supported Intermediate Temperature Solid Oxide Fuel Cell (Master's Thesis)*, Rensselaer Polytechnic Institute Hartford (2014)
15. B. E. Poling, J. M. Prausnitz, and J. P. O'Connell, *The Properties of Gases and Liquids*, 5th ed. New York: McGraw-Hill (2000)
16. B. Todd and J. B. Young, *Journal of Power Sources*, **110**, 186-200 (2002)
17. B. A. Haberman and J. B. Young, *Journal of Heat and Mass Transfer*, **47**, 3617-3629 (2004)
18. Y. Wang, F. Yoshiba, M. Kawase, and T. Watanabe, *International Journal of Hydrogen Energy*, **34**, 3885-3893 (2009)